Defect-rich AuCu@Ag nanowires with exclusive strain effect accelerate nitrate reduction to ammonia

Songliang Liu [a], Weixin Miao [a], Kun Ma [a], Huaifang Teng [a], Xu Zhang [a], Jialin Li [a], Wenzhen Li [b], Xuejing Cui [a], Luhua Jiang [a],*

[a] Electrocatalysis & Nanomaterial Laboratory, College of Materials Science and Engineering, Qingdao University of Science and Technology, Qingdao 266042, China
[b] Department of Chemical & Biological Engineering, Iowa State University, Ames, IA 50011-1098, United States

ABSTRACT

Electrocatalytic nitrate reduction to ammonia is an attractive alternative route for the traditional Haber-Bosch process, yet suffers from unsatisfied efficiency and selectivity due to multiple intermediates as well as the competitive hydrogen evolution reaction. Herein, we report a defect-rich AuCu@Ag nanowires (AuCu@Ag NWs) with exclusive strain effect as an efficient electrocatalyst for nitrate reduction reaction (NO_3^-RR). AuCu@Ag NWs catalyst shows excellent electrocatalytic performance for NO_3^- to NH_3 in the NO_3^-RR process, with the NH_3 yield rate of 975.1 μg h^{-1} $mg_{cat.}^{-1}$, Faraday efficiency of 96.9% and NH_3 selectivity of 95.7%. DFT theoretical investigation manifests that the Ag atomic shell deposited layer-by-layer on AuCu NWs generates exclusive strain effect that accelerates the adsorption of NO_3^- and reaction intermediates, thereby enhances the NO_3^-RR activity. This work opens up new avenues for rational construction of high-performance NO_3^-RR electrocatalysts by synergistically modulating the electronic configuration of the active atoms through defect and strain engineering.

1. Introduction

Ammonia (NH_3) is not only a raw material for fertilizers, drugs, and many chemicals, but also is considered as a green and clean energy carrier due to its high energy density (4.3 kW h kg^{-1}) [1–3]. The traditional NH_3 synthesis process relies on the Haber-Bosch method, which requires consumption of large amounts of fossil fuels to provide the high-temperature and high-pressure environments for breaking the stable N≡N bond [4–7]. It is urgent to develop green NH_3 synthesis technologies.

Nitrogen (N_2), from the viewpoint of availability, is the most ideal N source for the synthesis of NH_3 which therefore has received extensive attraction via the electrocatalytic route to convert N_2 to NH_3 that mimics the natural nitrogen fixation by microorganisms under ambient conditions has received much attention [8–13]. However, electrocatalytic conversion of N_2 to NH_3 still faces problems such as low solubility of N_2 in solution, high dissociation energy of N≡N (941 kJ mol^{-1}), and the strong competitive hydrogen evolution reaction (HER), so is hard to reach the industrial-level NH_3 production [14–17]. Nitrate (NO_3^-) has a relatively low N═O dissociation energy (204 kJ mol^{-1}) and good solubility compared to N_2 [18–20]. In addition, NO_3^- as a widespread

pollutant in waste water, it is an ideal choice to kill two birds with one stone by converting the waste NO_3^- into high value-added NH_3 [21–24]. Therefore, NO_3^- reduction reaction (NO_3^-RR) becomes a more attractive strategy for electrocatalytic nitrogen fixation. However, NO_3^-RR is not only a complex 8-electron transfer catalytic process but also contains multiple possible transformations of intermediate species [25–29]. Developing efficient electrocatalysts with both high activity and high Faraday efficiency (FE) remains a great challenge.

Transition metal (Cu, Ag and Co, etc.) based catalysts are considered to be one of the most efficient catalysts for NO_3^-RR [30–35]. In general, the catalytic activity and stability of transition metal-based catalysts for NO_3^-RR can be effectively enhanced by modifying the chemical composition and morphological structure. In terms of chemical composition, introducing of more stable atoms for alloying not only optimizes the electronic configuration of transition metals and enhances the structural stability, but also promotes the selective adsorption and activation of reactive intermediate species [36–38]. For example, Zhang and co-authors successfully prepared Ru_xCo_y hollow nano-dodecahedrons by alloying Ru with Co, in which the electrons transfer from Ru to Co leading to the downshift of the *d*-band center of Co atoms [39]. As a result, the adsorption and conversion of the intermediate

species NO_2^- on metal surface were optimized, which significantly enhanced the catalytic performance of NO_3^-RR. In terms of morphological structure, the one-dimensional nanowire structure not only possesses unique anisotropy and anti-aggregation ability, but also could provide continuous electron transfer pathways to reduce the charge transfer resistance, thus exhibiting enhanced catalytic performance [40–43]. In addition, it is an effective design strategy to optimize the catalytic performance by modulating the electronic configuration of catalysts through strain engineering by core-shell structures [44,45]. Guo and his co-workers constructed PdCu/Ir core-shell nanocrystals by precisely regulating the thickness of the Ir shell to generate unique compressive strains, which weakened the binding of reactive intermediate species and obtained enhanced catalytic activity.[46]. Besides the chemical composition and structural morphology of the materials, to create structural defects by defect engineering strategy could expose more surface atoms and unsaturated sites as active centers, possibly to significantly optimize the intrinsic activity and catalytic reaction kinetics [47–50]. Therefore, it is highly expected and promising to create ideal NO_3^-RR catalysts by elaborately designing catalyst morphology, compositions and surface structure.

Herein, a defect-rich AuCu@Ag nanowires (AuCu@Ag NWs) with exclusive strain effect is constructed collaboratively through defect engineering and strain engineering. The AuCu@Ag NWs takes advantages of (i) the surface Ag atoms perfectly replicate the structural defects of the inner AuCu nanowires (AuCu NWs), and (ii) the core-shell configuration introduces unique compressive strains. The AuCu@Ag NWs exhibits excellent NH_3 yield rate (r_{NH3}: 975.1 μg h^{-1} mg$_{cat.}^{-1}$) and FE (96.9%) for the NO_3^-RR, which is better than its counterparts, Ag nanowires (Ag NWs), AuCu NWs and AuCuAg nanowires (AuCuAg NWs). Density functional theory (DFT) calculations further show that the Ag shell not only upshifts the d-band center of the AuCu alloy to optimize the catalyst electronic configuration, but also brings compressive strain that plays a key role in improving the performance of NO_3^-RR.

2. Experimental section

2.1. Materials and chemicals

$HAuCl_4$, $CuCl_2·2 H_2O$, $AgNO_3$, 4-aminopyridine (4-AP), L-ascorbic acid (AA), KOH, NH_4Cl, $^{15}NH_4Cl$, KNO_3, $K^{15}NO_3$ and Nafion solution (5 wt%) were received from Sigma-Aldrich. HCl and ethanol were purchased from Beijing Chemical Works.

2.2. Synthesis of AuCu@Ag NWs

For a typical synthesis of AuCu@Ag NWs, 4-AP (47 mg) ultrasonically dissolved in 7 mL of ultrapure water. 1 mL of $HAuCl_4$ (20 mM), 1 mL of $CuCl_2·2 H_2O$ (20 mM) and 1 mL of AA (100 mM) were added to the above solution, mixed homogeneously and placed in an oil bath at 120 °C for 2 mins. Then added 1 mL of $AgNO_3$ (20 mM) and the reaction continue for 5 mins. The reaction was cooled to room temperature and washed 3 times by centrifugation alternating with ethanol and water.

2.3. Synthesis of AuCu NWs and AuCuAg NWs

AuCu NWs was prepared under typical conditions without the addition of $AgNO_3$. AuCuAg NWs was prepared by simultaneous addition of $HAuCl_4$, $CuCl_2·2 H_2O$ and $AgNO_3$ under typical conditions for 5 mins.

2.4. Synthesis of Ag NWs

1 mL of $AgNO_3$ (20 mM) was added to 5 mL freshly prepared $NaBH_4$ (20 mM) in an ice bath for 5 mins, and the products were collected by centrifugal washing.

3. Results and discussion

3.1. Synthesis and characterization of AuCu@Ag NWs

The preparation process for the defect-rich AuCu@Ag NWs and alloyed AuCuAg NWs is shown in Fig. 1a. During the synthesis process of AuCu NWs precursor and AuCuAg NWs, AA acts as a reducing agent, while 4-AP serves as a structure-directing agent that can form complex compounds with metal atoms to induce the formation of one-dimensional nanowire structures. The AuCu@Ag NWs was obtained by adding the Ag precursor ($AgNO_3$) to the mixed reaction solution containing AuCu NWs, where AuCu NWs acts as a template and on which epitaxially grows an Ag shell under the reduction of AA. The high-angle annular dark-field scanning transmission electron microscopy (HAADF-STEM) and transmission electron microscope (TEM) images show that the obtained AuCu NWs, AuCuAg NWs, and AuCu@Ag NWs all exhibit highly dispersed uniform nanowire structures (Fig. 1b–1d and S1). In addition, due to the epitaxial growth of the Ag shell, the average diameter of the prepared AuCu@Ag NWs is 2.95 nm, slightly larger than the average diameters of AuCu NWs (2.40 nm) and AuCuAg NWs (2.35 nm) (Fig. 1e–1g).

A representative set of high-resolution TEM (HRTEM) images was used to further investigate the microstructure of AuCu NWs, AuCuAg NWs, and AuCu@Ag NWs. As shown in Fig. 2a, AuCu NWs presents a significant Boerdijk-Coxeter helical structure (linearly stacked regular tetrahedrons with (111) dominant facets in different directions) with lattice spacing (0.226 nm) pointing towards the (111) planes of the face-centered cubic (*fcc*) AuCu alloy [51]. In addition, AuCu NWs expose abundant structural defects (grain boundary, stacking faults (blue arrows), atomic steps, and amorphous sites (red arrows)), which not only act as catalytic active centers but also could alter the electron transport channels and improve the electron transport efficiency (Fig. 2a) [52]. The false-color processed HRTEM images show the formation of the Boerdijk-Coxeter helical structure in a clearer way (Fig. 2b). The HAADF-STEM images and the corresponding energy dispersive X-ray (EDX) elemental patterns show that Au and Cu elements are uniformly distributed on the nanowires, further confirming the formation of the AuCu alloys (Fig. 2c). The EDX analysis of the AuCu NWs shows that the atomic ratio of Au:Cu is about 1:1 (Fig. S2). The AuCuAg NWs after introducing Ag atoms have the same Boerdijk-Coxeter helix structure and abundant structural defects as AuCu NWs, and the lattice spacing (0.231 nm) points to the (111) plane of the *fcc* AuCuAg alloy (Fig. 2d and 2e). EDX analysis of AuCuAg NWs shows that the atomic ratio of Au:Cu:Ag is about 1:1:1(Fig. 2f and S3).

It should be pointed that the epitaxially grown Ag shells of AuCu@Ag NWs perfectly replicate the Boerdijk-Coxeter helical structure and structural defects (grain boundary, twin boundary, stacking faults (blue arrows), atomic steps, and amorphous sites (red arrows)) of AuCu NWs (Fig. 3a and 3b). These perfectly replicated structural defects could effectively regulate the interatomic electronic structure and coordination environment, thereby optimizing the adsorption of reaction intermediates and improving catalytic performance [53,54]. The lattice spacing of the Ag shell (0.226 nm) remains consistent with the lattice spacing of AuCu NWs (0.226 nm), and the thickness of the Ag shell is approximately 2–3 atomic layers (Fig. 3a). The EDX analysis of AuCu@Ag NWs indicates that the atomic ratio of Au:Cu:Ag is almost identical to that of AuCuAg NWs, maintaining a ratio of 1:1:1 (Fig. 3c and S4). The normal Ag NWs was fabricated in one step using $NaBH_4$ as the reducing agent. The TEM images show that normal Ag NWs exhibit a uniform nanowire structure with a lattice spacing of 0.235 nm, consistent with that of the conventional Ag (JCPDS-65–2871) (Fig. S5). Interfacial lattice mismatch between the AuCu cores in the AuCu@Ag NWs and the Ag shells grown by surface epitaxy results in the Ag shells under compressive strain. According to the strain equation $\tau_{Ag} = (\alpha_{Ag} - \alpha_{shell})/\alpha_{shell}$, the compressive strain of the Ag shell (τ_{Ag}) is 3.98% [55]. In contrast, unlike the AuCu@Ag NWs where the Ag atoms grow epitaxially
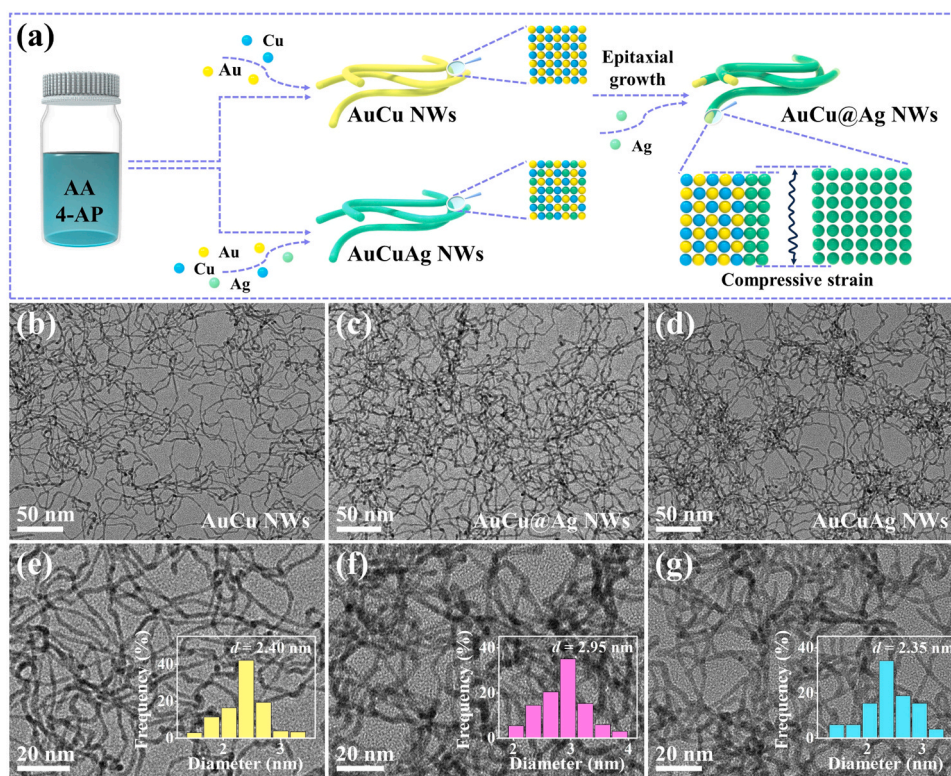
Fig. 1. (a) Schematic illustration for the synthesis of AuCu NWs, AuCuAg NWs and AuCu@Ag NWs. TEM images of the (b and e) AuCu NWs, (c and f) AuCuAg NWs and (d and g) AuCu@Ag NWs. The insets show the distribution of diameters for (e) AuCu NWs, (f) AuCuAg NWs and (g) AuCu@Ag NWs, respectively.
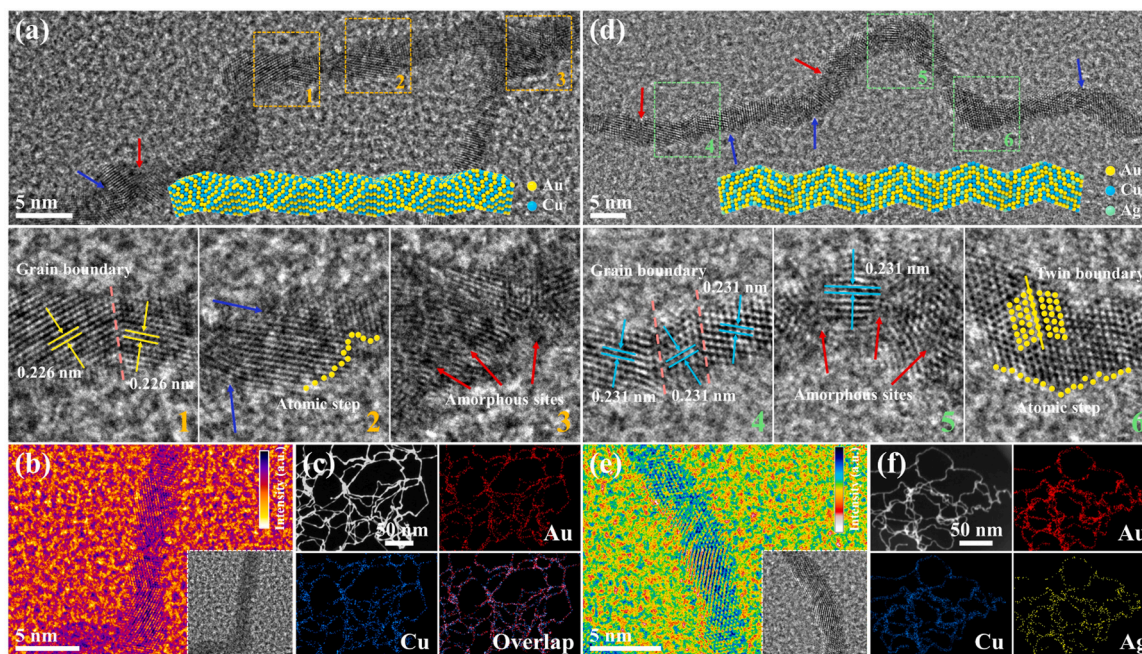

Fig. 2. HRTEM images of the (a) AuCu NWs and (d) AuCuAg NWs. False-color HRTEM images of the (b) AuCu NWs and (e) AuCuAg NWs. HAADF-STEM and EDS mapping images of the (c) AuCu NWs and (f) AuCuAg NWs. The insets show illustrations of the models for (a) AuCu NWs and (b) AuCuAg NWs, respectively.

over the AuCu core to form a core-shell configuration, the alloyed AuCuAg NWs with a perfect *fcc* crystal structure have random occupancy of Au, Cu, and Ag atoms, thereby significantly reducing the strain effect. The results indicate that the construction of the core-shell configuration can produce compressive lattice strain to optimize the interatomic electronic configurations, making AuCu@Ag NWs

potentially capable of further enhancing the electrocatalytic performance.

The crystal structures of AuCu@Ag NWs were further investigated by X-ray diffraction (XRD) analysis. AuCu NWs, AuCuAg NWs, and AuCu@Ag NWs all exhibit similar diffraction peaks of typical metallic *fcc* structures (Fig. S6). The diffraction peak positions of AuCu NWs are
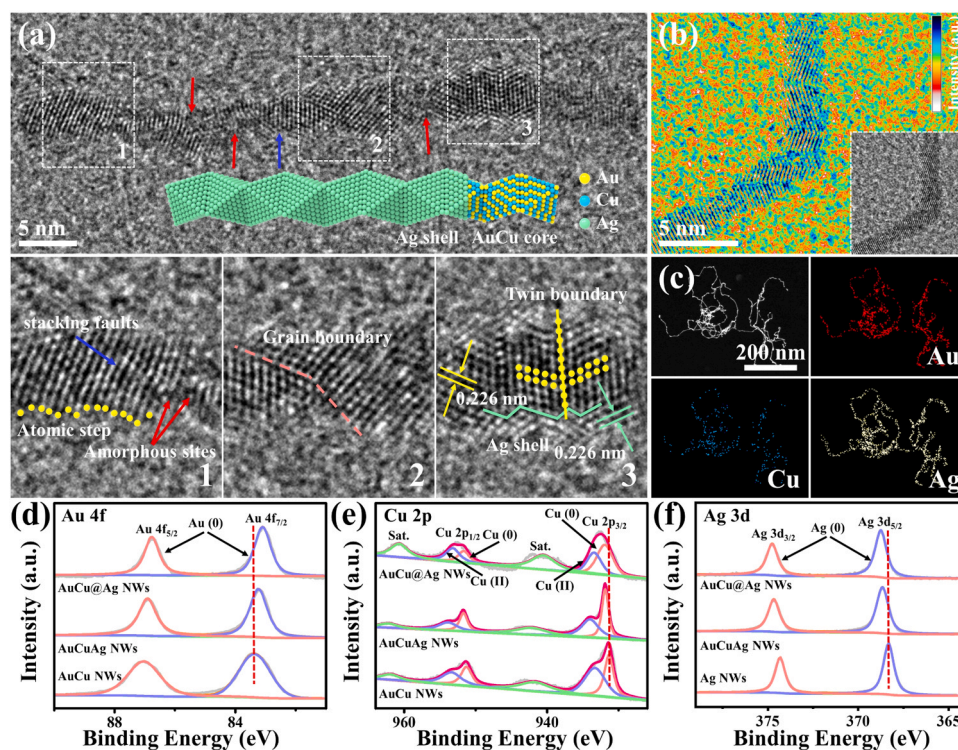
Fig. 3. (a) TEM image and (b) False-color HRTEM images of the AuCu@Ag NWs. (c) HAADF-STEM and EDS mapping images of the AuCu@Ag NWs. (d) XPS spectra of the Au 4 f peaks of AuCu NWs, AuCuAg NWs and AuCu@Ag NWs. (e) XPS spectra of the Cu 2p peaks of AuCu NWs, AuCuAg NWs and AuCu@Ag NWs. (f) XPS spectra of the Ag 3d peaks of AuCu NWs, AuCuAg NWs and AuCu@Ag NWs.

located between the derived peaks of standard *fcc* Au (JCPDS-65–8601) and standard Cu (JCPDS-04–0836), indicating lattice contraction, due to the introduction of Cu atoms into the Au atomic layers, and confirms the formation of the AuCu alloy. Furthermore, it is found that the position of the diffraction peaks of the alloy AuCuAg NWs shift towards low diffraction angle after introducing Ag atoms, which is attributed to lattice expansion with Ag atoms being introduced into the AuCu atomic layer. It is noteworthy that there is no significant change compared to the AuCu NWs in the position of the XRD peaks of the AuCu@Ag NWs after growing an Ag shell over the alloyed AuCu NWs, and also no additional phases could be detected. These results further indicate that Ag actually grows epitaxially on the surface of AuCu alloys with lattice spacing consistent with the inner AuCu core. The chemical composition and surface electronic states of AuCu@Ag NWs were further investigated by X-ray photoelectron spectroscopy (XPS) (Fig. S7). The XPS spectrum of Au 4 f can be divided into two sets of peaks, namely Au 4 $f_{5/2}$ and Au 4 $f_{7/2}$ (Fig. 3d). The XPS spectrum of Cu 2p can be divided into two sets of peaks as well, namely Cu $2p_{1/2}$ and Cu $2p_{3/2}$, further splitting into two doublets corresponding to the Cu(0) and Cu(II) chemical states (Fig. 3e). The small amount of Cu(II) may result from the oxidation of the material in air [56]. In addition, the peaks at 960.7 and 940.5 eV correspond to the satellite peaks of Cu $2p_{1/2}$ and Cu $2p_{3/2}$, respectively. The XPS spectrum of Ag 3d also exhibits two sets of peaks corresponding to Ag $3d_{3/2}$ and Ag $3d_{5/2}$ (Fig. 3f). All the atoms in the AuCu NWs, AuCuAg NWs, and AuCu@Ag NWs are predominantly in the metallic state. It is noteworthy that, compared to AuCu NWs, the binding energies of the Au 4 f spectrum in AuCuAg NWs and AuCu@Ag NWs negatively shifts to different extent, while the binding energies corresponding to the Cu 2p electrons shift positively, and the binding energies of Ag 3d electrons also positively shifts compared to Ag NWs. The peak shift of AuCu@Ag NWs is more intense than that of AuCuAg NWs, indicating that the core-shell configuration formed by the epitaxial growth of Ag atoms leads to significant change in the electronic structure of metal atoms. Such a change originates from the charge transfer

from Ag or Cu to Au, which is expected to enhance the adsorption of reactants and intermediates on the surface, thus optimizing the catalytic selectivity.

3.2. Electrocatalytic performances for NO_3^-RR

NO_3^-RR was performed in an Ar-saturated H-type electrolytic cell containing 0.1 M KOH + 50 mg L^{-1} NO_3^--N (the concentration is normalized to N) to evaluate the catalytic performance of AuCu@Ag NWs (Fig. 4a). Fig. 4b shows the LSV curves of AuCu@Ag NWs as a catalyst tested in 0.1 M KOH and 0.1 M KOH + 50 mg L^{-1} NO_3^--N. The LSV curves with the addition of NO_3^- show a significant increase in the current density at the same potential, which is mainly attributed to the reduction of NO_3^-, indicating that the NO_3^-RR can be effectively driven catalyzed by AuCu@Ag NWs. Subsequently, chronoamperometry (i-t) tests were conducted in Ar-saturated 0.1 M KOH + 50 mg L^{-1} NO_3^--N to further evaluate the performance of AuCu@Ag NWs for NO_3^-RR. The absorption intensity of reactants (NO_3^-) and products (NO_2^- and NH_3) in the electrolyte after the reaction were tested by UV–visible spectrophotometry, and quantitative analysis was further carried out according to the standard curves (Fig. S8-S10). As shown in Fig. 4c, NO_3^--N is almost completely converted in the potential interval from –0.2 V to –0.5 V (*vs.* RHE). In addition, the optimal r_{NH3} = 975.1 µg h^{-1} mg$_{cat.}^{-1}$, FE (96.9%) and NH_3 selectivity (95.7%) are achieved at –0.2 V (*vs.* RHE) (Fig. 4d and 4e). Meanwhile, we observed a sharp decrease in FE as the potential continued to decrease, mainly due to the rapid intervention of competitive HER. The concentration-time curves of NO_3^--N, NO_2^--N and NH_3-N were recorded within 2 h at a typical potential of –0.2 V (*vs.* RHE) (Fig. 4f). With the continuous progress of NO_3^-RR, the concentration of NO_3^--N in the electrolyte gradually decreases, while the concentration of NH_3-N continuously increases. In addition, the concentration of NO_2^--N was kept at a low value during the 2 h electrolysis process. The results indicate excellent NO_3^--N conversion and NH_3 selectivity throughout the entire NO_3^-RR reduction process under the catalytic
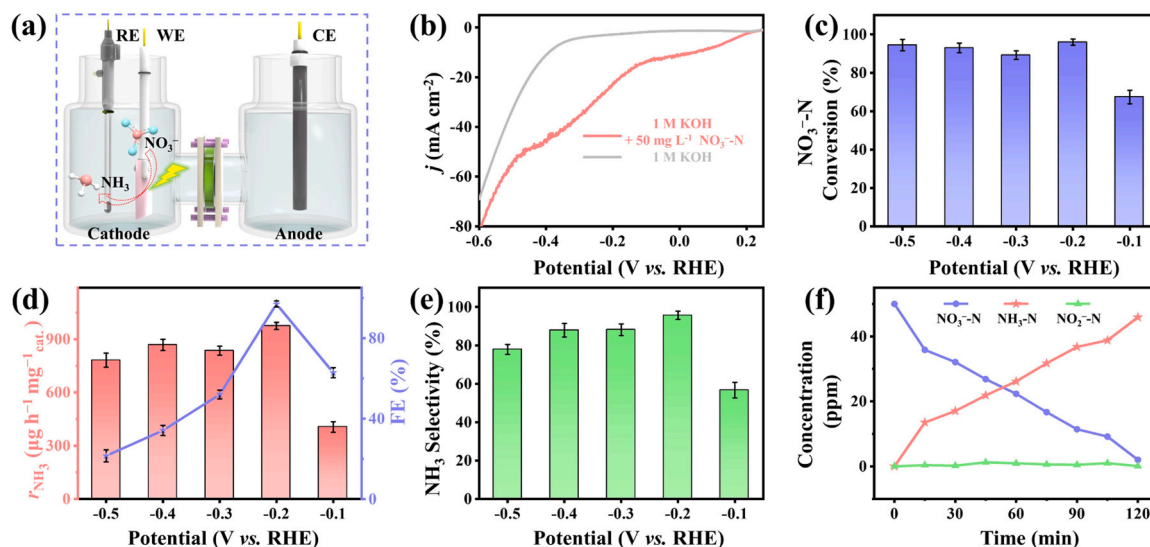
Fig. 4. (a) Schematic setup. (b) LSV curves of AuCu@Ag NWs in 1 M KOH with and without 50 mg L^{-1} NO$_3^-$-N. (c) The NO$_3^-$-N conversion rate, (d) r_{NH3} and corresponding FE and (e) NH$_3$ selectivity of AuCu@Ag NWs at different potentials. (f) The NO$_3^-$-N, NO$_2^-$-N and NH$_3$-N concentration versus different reaction time of the AuCu@Ag NWs at −0.2 V (*vs.* RHE).

action of AuCu@Ag NWs. It is worth noting that the performance of AuCu@Ag NWs for the NO$_3^-$RR ranks the top in the reported catalysts (Table S1).

In order to investigate the influence of compositional coordination effect and exclusive strain effect on NO$_3^-$RR properties due to epitaxial growth of Ag shells in AuCu@Ag NWs, the NO$_3^-$RR properties of AuCu NWs, AuCuAg NWs, and Ag NWs were investigated under the same conditions. As shown in Fig. 5a, the LSV curves of AuCu@Ag NWs tested in the presence of 50 mg L^{-1} NO$_3^-$-N exhibit the highest current density at the same potential, indicating that AuCu@Ag NWs has the best
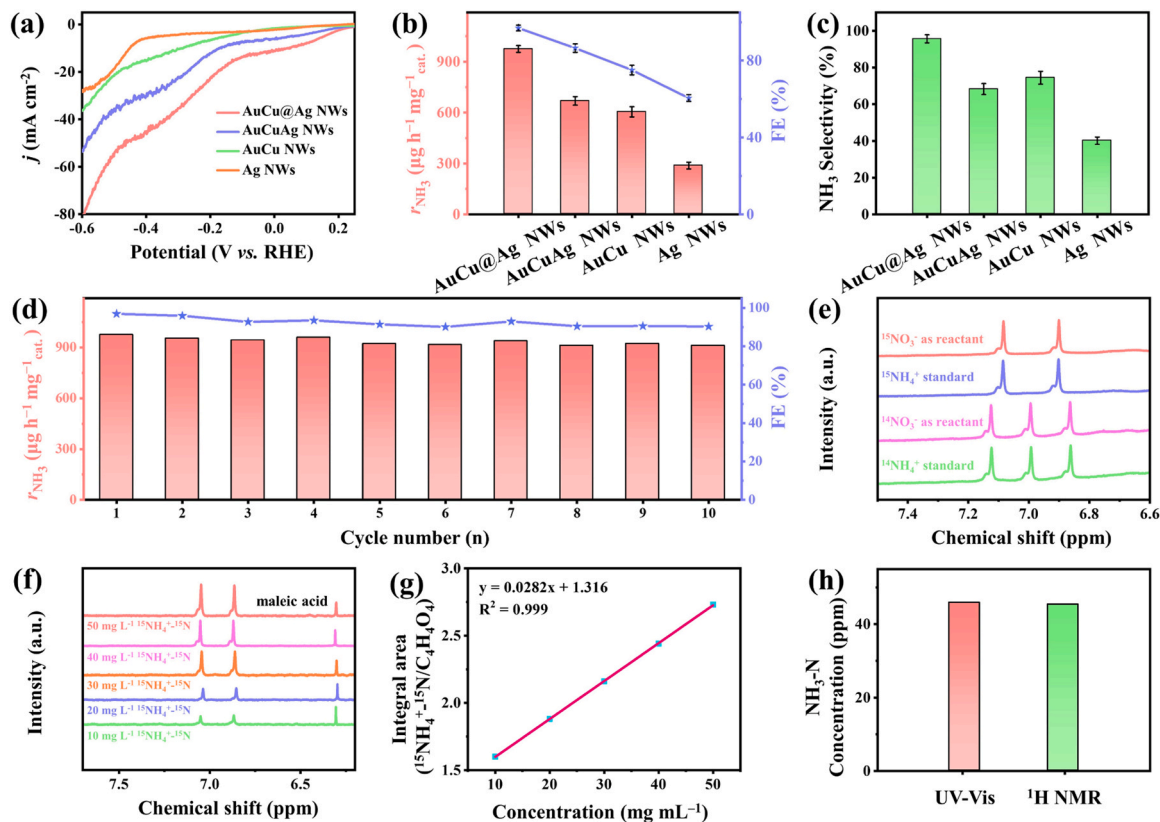

Fig. 5. (a) The LSV curves of Ag NWs, AuCu NWs, AuCuAg NWs and AuCu@Ag NWs in 1 M KOH + 50 mg L^{-1} NO$_3^-$-N. (b) The r_{NH3} and corresponding FE and (c) NH$_3$ selectivity of Ag NWs (−0.3 V (*vs.* RHE)), AuCu NWs (−0.3 V (*vs.* RHE)), AuCuAg NWs (−0.2 V (*vs.* RHE)) and AuCu@Ag NWs (−0.2 V (*vs.* RHE)). (d) The r_{NH3} and corresponding FE of AuCu@Ag NWs for consecutive cycles at −0.2 V (*vs.* RHE). (e) ^{1}H NMR spectra of ^{15}NH$_4^+$ standard solution, ^{14}NH$_4^+$ standard solution and the electrolyte after NO$_3^-$RR using ^{15}NO$_3^-$ and ^{14}NO$_3^-$ as the N source. (f) ^{1}H NMR spectra of ^{15}NH$_4^+$-^{15}N with different concentrations. (g) The standard curve of integral area (^{15}NH$_4^+$-^{15}N/C$_4$H$_4$O$_4$) against ^{15}NH$_4^+$-^{15}N concentration. (h) NH$_3$ concentration quantified by UV–vis (^{14}NO$_3^-$ as a reactant) and ^{1}H NMR (^{15}NO$_3^-$ as a reactant).

NO_3^-RR current response. The optimal potential for both AuCu@Ag NWs and AuCuAg NWs is –0.2 V (vs. RHE), while the optimal potential for AuCu NWs and Ag NWs is –0.3 V (vs. RHE). This suggests that introducing Ag into AuCu NWs can optimize the inter-component electronic configuration, thereby enhancing the NO_3^-RR current response and reducing energy consumption (Figs. 4c-4e and S11). Meanwhile, the r_{NH3}, FE and NH_3 selectivity of AuCu NWs (r_{NH3}: 604.3 µg h^{-1} mg$_{cat.}^{-1}$, FE: 75.1%, NH_3 selectivity: 74.4%), Ag NWs (r_{NH3}: 287.2 µg h^{-1} mg$_{cat.}^{-1}$, FE: 60.5%, NH_3 selectivity: 40.1%), and AuCuAg NWs (r_{NH3}: 668.8 µg h^{-1} mg$_{cat.}^{-1}$, FE: 86.5%, NH_3 selectivity: 68.3%) at the optimal potential are lower than those of AuCu@Ag NWs (r_{NH3}: 975.1 µg h^{-1} mg$_{cat.}^{-1}$, FE: 96.9%, NH_3 selectivity: 95.7%) (Figs. 5b and 5c). This result indicates that the compositional coordination effect and exclusive strain effect brought by the epitaxial growth of the Ag shell contribute more to the enhancement of NO_3^-RR performance than the sole compositional co-ordination effect resulting from the introduction of Ag atoms through alloying. In addition, we used electrochemical impedance spectroscopy (EIS) to analyze the electron transfer kinetics during the NO_3^-RR process. As shown in Fig. S12, AuCu@Ag NWs exhibits the smallest semicircle in the Nyquist plot, indicating a smaller charge transfer resistance of AuCu@Ag NWs than the other comparative catalysts, which contributes to the promoted NO_3^-RR process.[57] To further evaluate the catalytic stability of AuCu@Ag NWs, continuous 10 cycles of 2 h electrolysis tests

were performed at –0.2 V (vs. RHE). As shown in Fig. 5d, no significant changes for the r_{NH3} and FE in the 10 cycles. Furthermore, AuCu@Ag NWs maintains a dispersed nanowire-like structure after 10 cycles (Fig. S13). The results demonstrate that AuCu@Ag NWs exhibit excellent catalytic stability and structural stability for NO_3^-RR.

The source of N in the product NH_3 was determined by performing a set of blank control experiments to further eliminate any influence from the environmental N sources or electrodes on the reaction process by comparing the NH_3 concentration in electrolytes after 2 h- chronoamperometry tests in (1) At the AuCu@Ag NWs electrode in 1 M KOH; (2) at a blank carbon paper electrode in 1 M KOH + 50 mg L^{-1} NO_3^--N; (3) At the AuCu@Ag NWs electrode in open circuit potential; (4) blank electrolyte without electrolysis (Fig. S14). In the above control experiments, no significant NH_3 generation is detected except for AuCu@Ag NWs in 1 M KOH + 50 mg L^{-1} NO_3^--N, indicating that the final product NH_3 all originated from the NO_3^-RR driven by AuCu@Ag NWs. The origin of the N in the NH_3 was further confirmed by the ^{15}N isotope labeling experiments in 1 M KOH + 50 mg L^{-1} $^{15}NO_3^-$-^{15}N. As shown in Fig. 5e, the ^{1}H NMR spectra of the product NH_3 show a double peak of $^{15}NH_4^+$ and a triple peak of $^{14}NH_4^+$ in case that $^{15}NO_3^-$ and $^{14}NO_3^-$ were used as added electrolytes, respectively. In addition, we prepared a standard curve of $^{15}NH_4^+$ in the product using maleic acid ($C_4H_4O_4$) as an external standard for ^{1}H NMR, further quantitatively detecting NH_3 in
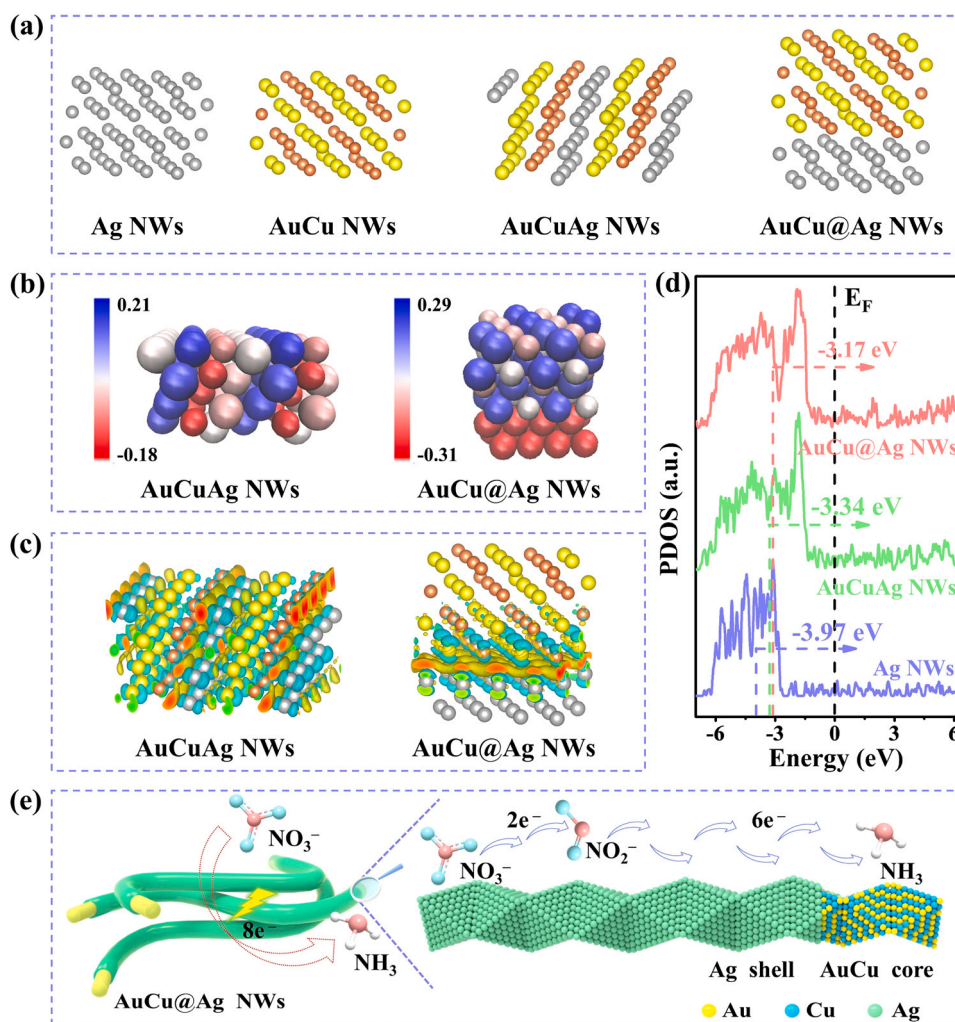

Fig. 6. (a) The geometric structure models for Ag NWs, AuCu NWs, AuCuAg NWs and AuCu@Ag NWs. (b) Bader charge of the AuCuAg NWs and AuCu@Ag NWs. Blue and red represent electron enrichment and electron deficiency, respectively. (c) The electron density difference on the AuCuAg NWs model and AuCu@Ag NWs model. (d) The PDOS of Ag NWs, AuCuAg NWs and AuCu@Ag NWs. (e) Schematic illustration showing the electrocatalytic NO_3^-RR mechanism over the AuCu@Ag NWs.

the product (Figs. 5f and 5g). The results of NH_3 concentration quantified by ^1H NMR spectroscopy using $^{15}NO_3^-$ as an additional electrolyte is almost identical to that quantified by the UV–vis spectroscopy using $^{14}NO_3^-$ as an additional electrolyte (Fig. 5h). The above results not only confirm the accuracy of the experimental results, but also further strongly demonstrated that the generated NH_3 in the electrolyte solution originated from NO_3^-RR.

To elucidate the NO_3^-RR mechanism over the unique AuCu@Ag NWs, the theoretical models of Ag NWs, AuCu NWs, AuCuAg NWs, and AuCu@Ag NWs are constructed and the electronic structures of metals are analyzed by the density functional theory (DFT) calculation (Fig. 6a). Bader charge analysis shows that Ag lose 1.159e in AuCuAg NWs and 0.250e in AuCu@Ag NWs, thus confirming that the introduction of Ag can alter the electronic structure of atoms in AuCu alloy (Fig. 6b and S15). After the introduction of Ag, the electrons are transferred from Ag and Cu atoms to Au atoms for both AuCuAg NWs and AuCu@Ag NWs, which results in negative charge characteristics of Ag and Cu atoms and the positive charge characteristics of Au atoms, which is consistent with the XPS results (Fig. 6c and S16). Further investigation of the projected density of states (PDOS) in the Ag *d*-band reveals that the the *d*-band center of AuCuAg NWs is significantly higher than that of Ag NWs due to the alloying-induced coordination effect. In addition, the *d*-band center of AuCu@Ag NWs remains high as compared to AuCuAg NWs, indicating that the exclusive strain effect and the compositional coordination effect generated between the Ag shell and AuCu core, synergistically optimize the electronic configuration of metals, creating a favorable local chemical environment for the adsorption of reactants and intermediate species (Fig. 6d). Therefore, the coordination effect between Ag shells and AuCu core, together with the exclusive strain effect induced by the Ag shells, synergistically optimizes the intermetallic electronic configuration, which contributes to the enhanced catalytic performance of AuCu@Ag NWs for NO_3^-RR.

Based on the above electrochemical analysis and the theoretical calculations, a possible mechanism for the selective synthesis of NH_3 via the NO_3^-RR process catalyzed by AuCu@Ag NWs is proposed (Fig. 6e). Compared with the counterparts, AuCu@Ag NWs possesses the synergistical advantages in both the core-shell structure and the multicomponent. Specifically, on the one hand, the AuCu core provides a stable substrate for Ag deposition, thus obtaining excellent structural stability. Expectedly, the Ag atoms perfectly replicate the structural defects of the AuCu core, thus bringing more abundant surface-active centers. On the other hand, the unique core-shell structure perfectly integrates the compositional coordination effect and the exclusive strain effect, which effectively alters the intermetallic electronic configuration, thereby enhancing the adsorption of reactant NO_3^- and intermediate species, and thus promoting the NO_3^-RR process kinetically.

4. Conclusion

In conclusion, a defect-rich AuCu@Ag NWs with exclusive strain effect is elaborately constructed by a surface engineering strategy, in which Ag is deposited layer-by-layer on AuCu NWs to perfectly replicate the defective structure of AuCu NWs. The unique AuCu@Ag NWs exhibits excellent performance for NO_3^-RR, with the NO_3^--N conversion rate of 95.9%, r_{NH3} of 975.1 μg h^{-1} mg$_{cat.}^{-1}$, FE of 96.9% and NH_3 selectivity of 95.7%. DFT calculations manifest that the component coordination effect and the exclusive strain effect between Ag shell and AuCu core synergistically optimize the intermetallic electronic structure, enhancing the adsorption of NO_3^- and reactive intermediate species and thus accelerating NO_3^-RR kinetics. This work not only provides a highly efficient catalyst for NO_3^-RR by manipulating the morphology, compositions and surface structure to modulate the electronic configuration of active centers, but also enriches the synthetic methodology of core-shell structured materials with exclusive strain effect, which could be applicable to synthesize versatile advanced materials.

CRediT authorship contribution statement

Luhua Jiang: Writing – review & editing, Visualization, Supervision, Funding acquisition. **Xu Zhang:** Software, Data curation. **Jialin Li:** Methodology, Formal analysis. **Wenzhen Li:** Visualization, Supervision, Software. **Xuejing Cui:** Visualization, Supervision, Software, Resources, Data curation. **Songliang Liu:** Writing – original draft, Supervision, Methodology, Investigation. **Weixin Miao:** Software, Investigation, Data curation. **Kun Ma:** Investigation, Data curation. **Huaifang Teng:** Software, Investigation.

Declaration of Competing Interest

The authors declare that they have no known competing financial interests or personal relationships that could have appeared to influence the work reported in this paper.

Data Availability

Data will be made available on request.

Appendix A. Supporting information

Supplementary data associated with this article can be found in the online version at doi:10.1016/j.apcatb.2024.123919.

References

[1] B.E.R. Snyder, A.B. Turkiewicz, H. Furukawa, M.V. Paley, E.O. Velasquez, M. N. Dods, J.R. Long, A ligand insertion mechanism for cooperative NH_3 capture in metal–organic frameworks, Nature 613 (2023) 287–291.

[2] J. Shao, H. Jing, P. Wei, X. Fu, L. Pang, Y. Song, K. Ye, M. Li, L. Jiang, J. Ma, R. Li, R. Si, Z. Peng, G. Wang, J. Xiao, Electrochemical synthesis of ammonia from nitric oxide using a copper–tin alloy catalyst, Nat. Energy 8 (2023) 1273–1283.

[3] W. He, J. Zhang, S. Dieckhöfer, S. Varhade, A.C. Brix, A. Lielpetere, S. Seisel, J.R. C. Junqueira, W. Schuhmann, Splicing the active phases of copper/cobalt-based catalysts achieves high-rate tandem electroreduction of nitrate to ammonia, Nat. Commun. 13 (2022) 1129.

[4] J. Liang, P. Liu, Q. Li, T. Li, L. Yue, Y. Luo, Q. Liu, N. Li, B. Tang, A.A. Alshehri, I. Shakir, P.O. Agboola, C. Sun, X. Sun, Amorphous boron carbide on titanium dioxide nanobelt arrays for high-efficiency electrocatalytic NO reduction to NH_3, Angew. Chem. Int. Ed. 61 (2022) e202202087.

[5] S. Ye, Z. Chen, G. Zhang, W. Chen, C. Peng, X. Yang, L. Zheng, Y. Li, X. Ren, H. Cao, D. Xue, J. Qiu, Q. Zhang, J. Liu, Elucidating the activity, mechanism and application of selective electrosynthesis of ammonia from nitrate on cobalt phosphide, Energy Environ. Sci. 15 (2022) 760–770.

[6] L. Zhang, H. Zhou, X. Yang, S. Zhang, H. Zhang, X. Yang, X. Su, J. Zhang, Z. Lin, Boosting electroreduction kinetics of nitrogen to ammonia via atomically dispersed Sn protuberance, Angew. Chem., Int. Ed. 62 (2023) e202217473.

[7] Y.-C. Wang, Z.-Z. Ma, Y.-F. Wu, X.-G. Wang, Preparation and properties of GCP-supported palladium particles composite towards electrochemical ammonia synthesis, J. Electrochem. 28 (2022) 2104091.

[8] S.-L. Meng, C. Zhang, C. Ye, J.-H. Li, S. Zhou, L. Zhu, X.-B. Li, C.-H. Tung, L.-Z. Wu, Cobaloximes: selective nitrite reduction catalysts for tandem ammonia synthesis, Energy Environ. Sci. 16 (2023) 1590–1596.

[9] L. He, L. Bao, X. He, J. Chen, X. Li, K. Dong, Z. Cai, S. Sun, D. Zheng, Y. Luo, Q. Liu, Z. Ren, M. Wu, X. Sun, Cobalt-nanoparticles-decorated 3D porous nitrogen-doped carbon network for electrocatalytic nitrite reduction to ammonia, Inorg. Chem. 62 (2023) 15352–15357.

[10] S. Liu, Y. Xu, S. Jiao, W. Tian, T. Zhou, Z. Wang, X. Li, L. Wang, H. Wang, Rational construction of Au$_3$Cu@Cu nanocages with porous core–shell heterostructured walls for enhanced electrocatalytic N_2 fixation, J. Mater. Chem. A 9 (2021) 8372–8377.

[11] X.-W. Zhang, G.-Y. Meng, L.-Q. Fang, D.-M. Chang, T. Li, J.-W. Hu, P. Chen, Y.-D. Liu, L.-H. Zhang, Intelligent control based on BP artificial neural network for electrochemical nitrate removal, J. Electrochem. 29 (2022) 211215.

[12] W. Gao, K. Xie, J. Xie, X. Wang, H. Zhang, S. Chen, H. Wang, Z. Li, C. Li, Alloying of Cu with Ru enabling the relay catalysis for reduction of nitrate to ammonia, Adv. Mater. 35 (2023) 2202952.

[13] S. Li, Y. Wang, Y. Du, X.D. Zhu, J. Gao, Y.C. Zhang, G. Wu, P-Block Metal-based electrocatalysts for nitrogen reduction to ammonia: a minireview, Small 19 (2023) 2206776.

[14] X. Shen, S. Liu, X. Xia, M. Wang, H. Ji, Z. Wang, J. Liu, X. Zhang, C. Yan, T. Qian, Interfacial microextraction boosting nitrogen feed for efficient ambient ammonia synthesis in aqueous electrolyte, Adv. Funct. Mater. 32 (2022) 2109422.

[15] X. Wu, M. Nazemi, S. Gupta, A. Chismar, K. Hong, H. Jacobs, W. Zhang, K. Rigby, T. Hedtke, Q. Wang, E. Stavitski, M.S. Wong, C. Muhich, J.-H. Kim, Contrasting capability of single atom palladium for thermocatalytic versus electrocatalytic nitrate reduction reaction, ACS Catal. 13 (2023) 6804–6812.

[16] S. Liu, Z. Wang, H. Zhang, S. Wang, P. Wang, Y. Xu, X. Li, L. Wang, H. Wang, Palladium nanothorn assembly array for efficient electroreduction of nitrogen to ammonia, ACS Sustain. Chem. Eng. 8 (2020) 14228–14233.

[17] Y. Chen, S. Gu, W. Li, Solid-electrolyte interphases enable efficient Li-mediated ammonia electrosynthesis, Joule 6 (2022) 1973–1976.

[18] Y. Chen, P. Ammari-Azar, H. Liu, J. Lee, Y. Xi, M.J. Castellano, S. Gu, W. Li, Sustainable waste-nitrogen upcycling enabled by low-concentration nitrate electrodialysis and high-performance ammonia electrosynthesis, EES Catal. 1 (2023) 504–515.

[19] L. Sun, H. Yao, Y. Wang, C. Zheng, B. Liu, Mesostructures engineering to promote selective nitrate-to-ammonia electroreduction, Adv. Energy Mater. 13 (2023) 2303054.

[20] Q.L. Hong, B. Sun, X. Ai, X.L. Tian, F.M. Li, Y. Chen, Au nanocrystals modified holey PtTeAu metallene heteronanostructures for plasmon-enhanced nitrate electroreduction, Adv. Funct. Mater. (2023) 2310730.

[21] Y. Xu, Y. Wen, T. Ren, H. Yu, K. Deng, Z. Wang, X. Li, L. Wang, H. Wang, Engineering the surface chemical microenvironment over CuO nanowire arrays by polyaniline modification for efficient ammonia electrosynthesis from nitrate, Appl. Catal. B: Environ. 320 (2023) 121981.

[22] J. Lim, D.A. Cullen, E. Stavitski, S.W. Lee, M.C. Hatzell, Atomically ordered PdCu electrocatalysts for selective and stable electrochemical nitrate reduction, ACS Energy Lett. 8 (2023) 4746–4752.

[23] N. Zhang, J. Shang, X. Deng, L. Cai, R. Long, Y. Xiong, Y. Chai, Governing interlayer strain in bismuth nanocrystals for efficient ammonia electrosynthesis from nitrate reduction, ACS Nano 16 (2022) 4795–4804.

[24] H. Liu, Y. Chen, J. Lee, S. Gu, W. Li, Ammonia-mediated CO₂ capture and direct electroreduction to formate, ACS Energy Lett. 7 (2022) 4483–4489.

[25] Y. Xu, K. Ren, T. Ren, M. Wang, Z. Wang, X. Li, L. Wang, H. Wang, Ultralow-content Pd in-situ incorporation mediated hierarchical defects in corner-etched Cu₂O octahedra for enhanced electrocatalytic nitrate reduction to ammonia, Appl. Catal. B: Environ. 306 (2022) 121094.

[26] T. Ren, Z. Yu, H. Yu, K. Deng, Z. Wang, X. Li, H. Wang, L. Wang, Y. Xu, Interfacial polarization in metal-organic framework reconstructed Cu/Pd/CuOₓ multi-phase heterostructures for electrocatalytic nitrate reduction to ammonia, Appl. Catal. B: Environ. 318 (2022) 121805.

[27] X. Zhang, C. Wang, Y. Guo, B. Zhang, Y. Wang, Y. Yu, Cu clusters/TiO₂₋ₓ with abundant oxygen vacancies for enhanced electrocatalytic nitrate reduction to ammonia, J. Mater. Chem. A 10 (2022) 6448–6453.

[28] Y. Huang, C. He, C. Cheng, S. Han, M. He, Y. Wang, N. Meng, B. Zhang, Q. Lu, Y. Yu, Pulsed electroreduction of low-concentration nitrate to ammonia, Nat. Commun. 14 (2023) 7368.

[29] T. Ren, Z. Duan, H. Wang, H. Yu, K. Deng, Z. Wang, H. Wang, L. Wang, Y. Xu, Electrochemical co-production of ammonia and biodegradable polymer monomer glycolic acid via the co-electrolysis of nitrate wastewater and waste plastic, ACS Catal. 13 (2023) 10394–10404.

[30] S. Liu, L. Cui, S. Yin, H. Ren, Z. Wang, Y. Xu, X. Li, L. Wang, H. Wang, Heterointerface-triggered electronic structure reformation: Pd/CuO nano-olives motivate nitrite electroreduction to ammonia, Appl. Catal. B: Environ. 319 (2022) 121876.

[31] P. Li, R. Li, Y. Liu, M. Xie, Z. Jin, G. Yu, Pulsed Nitrate-to-ammonia electroreduction facilitated by tandem catalysis of nitrite intermediates, J. Am. Chem. Soc. 145 (2023) 6471–6479.

[32] Y. Bu, C. Wang, W. Zhang, X. Yang, J. Ding, G. Gao, Electrical pulse-driven periodic self-repair of Cu-Ni tandem catalyst for efficient ammonia synthesis from nitrate, Angew. Chem., Int. Ed. 62 (2023) e202217337.

[33] Q. Liu, G. Wen, D. Zhao, L. Xie, S. Sun, L. Zhang, Y. Luo, A. Ali Alshehri, M. S. Hamdy, Q. Kong, X. Sun, Nitrite reduction over Ag nanoarray electrocatalyst for ammonia synthesis, J. Colloid Interf. Sci. 623 (2022) 513–519.

[34] H.-Y. Yang, K.-Y. He, X. Ai, X. Liu, Y. Yang, S.-B. Yin, P.-J. Jin, Y. Chen, Pyridine functionalized silver nanosheets for nitrate electroreduction, J. Mater. Chem. A 11 (2023) 16068–16073.

[35] K. Fan, W. Xie, J. Li, Y. Sun, P. Xu, Y. Tang, Z. Li, M. Shao, Active hydrogen boosts electrochemical nitrate reduction to ammonia, Nat. Commun. 13 (2022) 7958.

[36] L. Sun, H. Yao, F. Jia, Y. Wang, B. Liu, Intermediate confinement for selective ammonia electrosynthesis from nitrate on robust mesoporous metal catalysts, Adv. Energy Mater. 13 (2023) 2302274.

[37] J.-Y. Fang, Q.-Z. Zheng, Y.-Y. Lou, K.-M. Zhao, S.-N. Hu, G. Li, O. Akdim, X.-Y. Huang, S.-G. Sun, Ampere-level current density ammonia electrochemical synthesis using CuCo nanosheets simulating nitrite reductase bifunctional nature, Nat. Commun. 13 (2022) 7899.

[38] G.A. Cerrón-Calle, A.S. Fajardo, C.M. Sánchez-Sánchez, S. Garcia-Segura, Highly reactive Cu-Pt bimetallic 3D-electrocatalyst for selective nitrate reduction to ammonia, Appl. Catal. B: Environ. 302 (2022) 120844.

[39] S. Han, H. Li, T. Li, F. Chen, R. Yang, Y. Yu, B. Zhang, Ultralow overpotential nitrate reduction to ammonia via a three-step relay mechanism, Nat. Catal. 6 (2023) 402–414.

[40] Q. Xue, H. Huang, J.-Y. Zhu, Y. Zhao, F.-M. Li, P. Chen, Y. Chen, Au@Rh core-shell nanowires for hydrazine electrooxidation, Appl. Catal. B: Environ. 278 (2020) 119269.

[41] M. Li, Z. Zhao, T. Cheng, A. Fortunelli, C.-Y. Chen, R. Yu, Q. Zhang, L. Gu, B. V. Merinov, Z. Lin, Ultrafine jagged platinum nanowires enable ultrahigh mass activity for the oxygen reduction reaction, Science 354 (2016) 1414–1419.

[42] S. Liu, H. Ren, S. Yin, H. Zhang, Z. Wang, Y. Xu, X. Li, L. Wang, H. Wang, Defect-rich ultrathin AuPd nanowires with Boerdijk–Coxeter structure for oxygen reduction electrocatalysis, Chem. Eng. J. 435 (2022) 134823.

[43] X. Jiang, X. Qiu, G. Fu, J. Sun, Z. Huang, D. Sun, L. Xu, J. Zhou, Y. Tang, Highly simple and rapid synthesis of ultrathin gold nanowires with (111)-dominant facets and enhanced electrocatalytic properties, J. Mater. Chem. A 6 (2018) 17682–17687.

[44] S. Zhu, Y. Liu, Y. Gong, Y. Sun, K. Chen, Y. Liu, W. Liu, T. Xia, Q. Zheng, H. Gao, H. Guo, R. Wang, Boosting bifunctional catalysis by integrating active faceted intermetallic nanocrystals and strained Pt–Ir functional shells, Small (2023) 2305062.

[45] T. Li, Q. Wang, J. Wu, Y. Sui, P. Tang, H. Liu, W. Zhang, H. Li, Y. Wang, A. Cabot, J. Liu, Strain and shell thickness engineering in Pd₃Pb@Pt bifunctional electrocatalyst for ethanol upgrading coupled with hydrogen production, Small (2023) 2306178.

[46] M. Li, Z. Zhao, Z. Xia, M. Luo, Q. Zhang, Y. Qin, L. Tao, K. Yin, Y. Chao, L. Gu, W. Yang, Y. Yu, G. Lu, S. Guo, Exclusive strain effect boosts overall water splitting in PdCu/Ir core/shell nanocrystals, Angew. Chem., Int. Ed. 60 (2021) 8243–8250.

[47] S. Liu, H. Zhang, H. Yu, K. Deng, Z. Wang, Y. Xu, L. Wang, H. Wang, Tailored design of PdRh bimetallic nanoribbons by solvent-induced strategy for efficient alkaline hydrogen evolution, Appl. Catal. B: Environ. 336 (2023) 122948.

[48] K. Deng, W. Wang, Z. Lian, H. Yu, Z. Wang, Y. Xu, H. Wang, L. Wang, A general synthesis of crystal phase controllable aerogels for efficient hydrogen evolution, Small 19 (2023) 2304181.

[49] Q. Mao, X. Mu, W. Wang, K. Deng, H. Yu, Z. Wang, Y. Xu, L. Wang, H. Wang, Atomically dispersed Cu coordinated Rh metallene arrays for simultaneously electrochemical aniline synthesis and biomass upgrading, Nat. Commun. 14 (2023) 5679.

[50] K. Deng, Z. Lian, W. Wang, J. Yu, H. Yu, Z. Wang, Y. Xu, L. Wang, H. Wang, Lattice strain and charge redistribution of Pt cluster/Ir metallene heterostructure for ethylene glycol to glycolic acid conversion coupled with hydrogen production, Small 20 (2023) 2305000.

[51] R. Mendoza-Cruz, L. Bazán-Díaz, J.J. Velázquez-Salazar, G. Plascencia-Villa, D. Bahena-Uribe, J. Reyes-Gasga, D. Romeu, G. Guisbiers, R. Herrera-Becerra, M. José-Yacamán, Helical growth of ultrathin gold–copper nanowires, Nano Lett. 16 (2016) 1568–1573.

[52] D. Wang, X. Jiang, Z. Lin, X. Zeng, Y. Zhu, Y. Wang, M. Gong, Y. Tang, G. Fu, Ethanol-induced hydrogen insertion in ultrafine IrPdH boosts pH-universal hydrogen evolution, Small 18 (2022) 2204063.

[53] K. Deng, Q. Mao, W. Wang, P. Wang, Z. Wang, Y. Xu, X. Li, H. Wang, L. Wang, Defect-rich low-crystalline Rh metallene for efficient chlorine-free H₂ production by hydrazine-assisted seawater splitting, Appl. Catal. B: Environ. 310 (2022) 121338.

[54] B. Zhang, J. Zhang, M. Hua, Q. Wan, Z. Su, X. Tan, L. Liu, F. Zhang, G. Chen, D. Tan, X. Cheng, B. Han, L. Zheng, G. Mo, Highly electrocatalytic ethylene production from CO₂ on nanodefective Cu nanosheets, J. Am. Chem. Soc. 142 (2020) 13606–13613.

[55] H. Guo, L. Li, Y. Chen, W. Zhang, C. Shang, X. Cao, M. Li, Q. Zhang, H. Tan, Y. Nie, L. Gu, S. Guo, Precise strain tuning boosts electrocatalytic hydrogen generation, Adv. Mater. 35 (2023) 2302285.

[56] M. Wang, H. Chen, M. Wang, J. Wang, Y. Tuo, W. Li, S. Zhou, L. Kong, G. Liu, L. Jiang, G. Wang, Tuning C₁/C₂ Selectivity of CO₂ electrochemical reduction over in-situ evolved CuO/SnO₂ heterostructure, Angew. Chem. Int. Ed. 62 (2023) e202306456.

[57] T. Ren, Z. Yu, H. Yu, K. Deng, Z. Wang, X. Li, H. Wang, L. Wang, Y. Xu, Sustainable ammonia electrosynthesis from nitrate wastewater coupled to electrocatalytic upcycling of polyethylene terephthalate plastic waste, ACS Nano 17 (2023) 12422–12432.